**Journal of Minerals and Materials Characterization and Engineering, 2015, 3, 15-25**
Published Online January 2015 in SciRes. http://www.scirp.org/journal/jmmce
http://dx.doi.org/10.4236/jmmce.2015.31003

# Nucleation of Fe-Rich Intermetallic Phases on $\alpha$-$Al_2O_3$ Oxide Films in Al-Si Alloys

**Pilar Orozco-González[1*], Manuel Castro-Román[2], Simitrio Maldonado-Ruíz[1], Sergio Haro-Rodríguez[1], Fabián Equihua-Guillén[3], Rodrigo Muñiz-Valdez[3], Salvador Luna-Álvarez[3], Miguel Montoya-Dávila[1], Alejandra Hernández-Rodríguez[2]**

[1]Academic Unit of Engineering, Autonomous University of Zacatecas, Zacatecas, México
[2]CINVESTAV Saltillo, Saltillo, México
[3]Faculty of Engineering, Autonomous University of Coahuila, México
Email: orozco_pilar@yahoo.com.mx

Received 5 September 2014; revised 7 October 2014; accepted 14 October 2014



## Abstract

**Nucleation of Fe-rich intermetallic phases on $\alpha$-$Al_2O_3$ oxide films was analyzed in five experimental Al-Fe-Mn-Si alloys. In an attempt to verify the role of $\alpha$-$Al_2O_3$ films in nucleating Fe-rich intermetallics, experiments have been conducted under conditions where formed in situ oxide films were present. Some Fe-rich intermetallics are observed to be related with the oxide films in the microstructure, the present results are in accordance with some research that suggest that the Fe-rich intermetallic phases nucleate upon the oxide films. The intermetallic phases and $\alpha$-$Al_2O_3$ films were unambiguously identified with the help of complementary techniques such as thermal analysis, SEM/EDS and X-ray diffraction.**

## Keywords

**Aluminum Alloys, Intermetallics, Nucleation, Crystal Growth, Oxide Films**

## 1. Introduction

Iron is known to be the most common and at the same time the most detrimental impurity in Al-Si alloys due to its role in the formation of brittle Fe-rich intermetallic phases that precipitate during solidification process. In

*Corresponding author.

**How to cite this paper:** Orozco-González, P., *et al*. (2015) Nucleation of Fe-Rich Intermetallic Phases on $\alpha$-$Al_2O_3$ Oxide Films in Al-Si Alloys. *Journal of Minerals and Materials Characterization and Engineering*, **3**, 15-25.
http://dx.doi.org/10.4236/jmmce.2015.31003

this way, commercial Al-Si alloys always contain Fe impurities; this undesirable contamination is inevitable and cannot be economically removed from the molten aluminum, it comes either from the use of steel tools for melting and casting or from the use of scrap as the initial material.

The Fe impurities have a detrimental effect on the mechanical properties and extrusion characteristics of the Al-Si alloys. This is attributed to the formation of different Fe-containing intermetallic phases, such as $\alpha$-AlFeSi and $\beta$-AlFeSi [1]-[5]. The $\alpha$ phase is usually described as having a cubic, $\alpha_c$-$Al_{15}(Fe,Mn)_3Si_2$, [6] [7] or hexagonal, $\alpha_h$-$Al_8Fe_2Si$, [8]-[10] crystal structure, and the $\beta$ phase is generally considered to be monoclinic $Al_5FeSi$ [11]-[15]. Techniques have to be developed to neutralize the detrimental effect of Fe impurities: 1) rapid solidification; 2) manganese addition; 3) melt superheating; and 4) inclusion particles addition. The three first methods basically convert the crystallization of the $\beta$ phase to the less harmful Chinese script form, $\alpha_c$ phase [3] [8]. Each one of these methods has its own advantages and limitations.

The inclusion particles addition technique is based on the work performed by Campbell and co-workers [16]-[18]. They have reported that the Fe-rich intermetallic phases nucleate and grow on the wetted surfaces of the oxide films, which have long been identified as cracks in the castings. Campbell *et al.* have further applied this nucleation mechanism to explain the cracks observed along the central axis of some Fe-rich intermetallics and for remove oxide films from the liquid aluminum. According to Cao and Campbell [17] [18], the wet side of the oxide films acts as a preferential nucleation site for Fe-rich intermetallic phases. As these particles have an increased sedimentation tendency, they sink to the bottom, bringing the oxide films with them.

The nucleation of Fe-intermetallic phases, such as $\alpha$ and $\beta$, was reported to be enhanced in the presence of particular inclusions added such as $\alpha$-$Al_2O_3$ and $MgAl_2O_4$ [19]. Khalifa *et al*. [20] have investigated the nucleation of Fe-intermetallic phases on the surface of different inclusions. They have reported that some inclusions exhibit higher potency for the nucleation of particular Fe-intermetallic phases under certain conditions and poor potency under other conditions. In general, these results showed limited effect of the inclusion particles added on the nucleation of Fe-intermetallic phases. For example, $\gamma$-$Al_2O_3$, which is a potent nucleant for the primary phase $\alpha$-Al, exhibit poor potency for the nucleation of the Fe-intermetallic phases. On the other hand, Lu and Dahle [21] did not find direct physical contact between Fe-rich intermetallic phases and the oxide films, thus the role of the oxide films as a heterogeneous substrate of Fe-intermetallics is uncertain.

The present work was performed to provide additional experimental information about the interaction between the Fe-intermetallic phases and $\alpha$-$Al_2O_3$ oxide films, commonly present in Al-Si alloys, in order to clarify the role of this oxide as heterogeneous substrate for the nucleation of Fe-intermetallic phases. This aspect would aid in controlling intermetallic formation, allowing control of the microstructure of the castings and hence improvement of the mechanical properties of the commercial Al-Si alloys. It is worth mentioning that any intermetallic phase formation on $\gamma$-$Al_2O_3$ films was not investigated in this work.

## 2. Experimental Details

### 2.1. Melt Preparation

The chemical composition of the alloys, determined by inductively coupled plasma emission spectroscopy (ICP), is shown in **Table 1**. These alloys were prepared starting from aluminum ingots of commercial purity (99.79%); the main impurities present in these ingots were: 0.14% Fe and 0.05% Si. The added alloying elements were: Fe (99.98%), Mn (99.95%), and silicon of commercial grade. The chemical composition is given in weight percentage unless otherwise specified.

### 2.2. Thermal Analysis (TA)

To determine the solidification sequence and the onset reaction temperature, $T_p$, for the intermetallic phase formation (see **Table 2**), thermal analysis curves were obtained by employing an experimental device similar to the one used by Bäckerud *et al*. [5]. First, the alloy was melted and heated to 800˚C under ambient air conditions in a gas furnace. Subsequently, the melt was poured into a graphite cup having a wall thickness of 6 mm, which was preheated to 900˚C in an electric furnace; to achieve thermal equilibrium conditions, the melt was kept at 900˚C for 120 s in the graphite cup inside the electrical furnace. Finally, the sample was cooled down to room temperature at a rate of ~1˚C/s.

The alloy's temperature was measured with two K-type thermocouples placed on the graphite cup's lid, as shown in **Figure 1**. The precision of the thermocouples was assessed by measuring the melting temperature of

**Table 1.** Chemical composition of the aluminum alloys.

| Alloy | Al | Si | Mn | Fe | Fe/Mn ratio |
|---|---|---|---|---|---|
| 1 | 85.4 | 13.3 | 1.2 | 0.1 | 0.1 |
| 2 | 84.2 | 13.5 | 1.1 | 1.2 | 1.1 |
| 3 | 81.1 | 13.4 | 1.1 | 4.4 | 4.0 |
| 4 | 78.2 | 13.5 | 1.2 | 7.1 | 5.9 |
| 5 | 75.1 | 13.6 | 1.2 | 10.1 | 8.4 |

**Table 2.** Chemical composition and structural data of extracted intermetallic phases, determined from the results of the SEM/EDS and XRD analyses.

| Alloy | $T_p$ ˚C | $T_s$ ˚C | AlFeMnSi Intermetallic | Composition from SEM/EDS[a] | | | | Fe/Mn Weight Ratio | Formula | Lattice Parameter (Å) |
|---|---|---|---|---|---|---|---|---|---|---|
| | | | | Al | Si | Fe | Mn | | | |
| 1 | 610 | 595 | $\alpha_{sc}$ | 56.90 | 10.69 | 3.45 | 28.95 | 0.12 | $Al_{34.1}FeMn_{8.5}Si_{6.16}$ | $a$ = 12.648 |
| 2 | 655 | 640 | $\alpha_{bcc}$ | 58.20 | 10.24 | 9.77 | 21.80 | 0.45 | $Al_{12.3}FeMn_{2.27}Si_{2.1}$ | $a$ = 12.603 |
| 3 | 679 | 664 | $\alpha_{bcc}$ | 57.93 | 10.07 | 18.61 | 13.38 | 1.39 | $Al_{8.8}Fe_{1.36}MnSi_{1.47}$ | $a$ = 12.535 |
| 4 | 732 | 717 | $\alpha_{h}$ | 53.27 | 12.51 | 26.46 | 7.76 | 3.41 | $Al_{14}Fe_{3.36}MnSi_{3.15}$ | $a$ = 12.39, $c$ = 26.203 |
| 5 | 745 | 730 | $\alpha_{h}$ | 53.98 | 12.71 | 26.92 | 6.38 | 4.22 | $Al_{17.2}Fe_{4.15}MnSi_{3.9}$ | $a$ = 12.359, $c$ = 26.14 |

$T_p$—Onset temperature for the intermetallic phase formation; $T_s$—Isothermal treatment temperature. [a]Average of eight SEM/EDS analyses of the extracted particles, for each alloy.

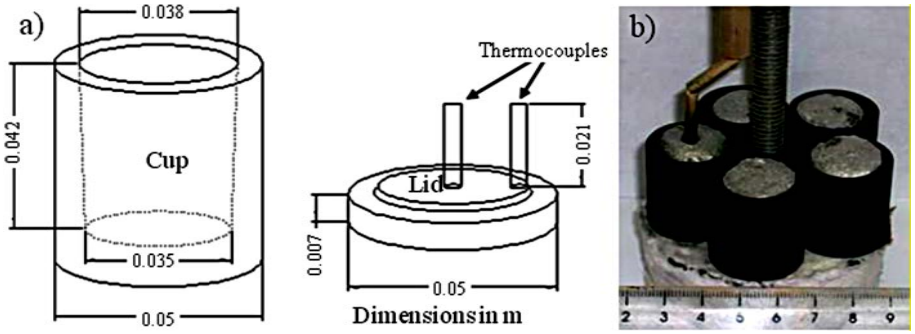


**Figure 1.** (a) Schematic illustration of the graphite cup and lid used to carry out the thermal analysis experiments; (b) Experimental setup used for the isothermal treatments.

pure aluminum 660.4˚C. The temperature-time data were recorded using a 16-bit resolution Daq Temp 14A card linked to a computer.

## 2.3. Isothermal Treatments

Based on the values of $T_p$ obtained for the formed intermetallics (see **Table 2**), the alloys were subjected to an isothermal treatment at a temperature set ~15˚C below $T_p$, which is hereinafter denominated as $T_s$. The purpose of this isothermal treatment was to allow the intermetallic particles to grow and settle down toward the bottom of the sample. Each sample was 19 mm in diameter and 25 mm in height and was placed inside a graphite crucible having a wall thickness of 3 mm. A set of five crucibles, shown in **Figure 1**, was heated in an electric furnace under ambient environment at 900˚C for 1800 s, subsequently cooled down to $T_s$ at ~1˚C/s and then held at $T_s$ for 15 hours. At the end of the isothermal treatment, the samples were quenched in a water bath at 25˚C. Due to the small size of the samples, the water quenching effectively retained the solid-liquid microstructure. Finally, the formed intermetallics were extracted by dissolving the aluminum matrix in a 15% (V/V) HCl aqueous solution.

### 2.4. Differential Thermal Analysis (DTA)

In order to provide microstructural evidence indicating the nucleation relationship between Fe-rich phases and oxide films, experiments were carried out in a DTA apparatus model 7 (Perkin Elmer). Round samples with weights of about 0.06 g were taken from the alloys. The measurements were carried out in the range of 400 to 900˚C with a heating and cooling rate of 0.083˚C/s under ambient air conditions. The temperature was measured with Pt-Pt/Rh thermocouples and the thermocouples' precision was assessed by measuring the melting temperature of pure aluminum 660.5˚C.

### 2.5. Characterization of Intermetallics

Extracted intermetallic particles were characterized in a JEOL JSM-6300 scanning electron microscope (SEM) equipped with an energy dispersive X-ray spectrometer (EDS). EDS spectra were recorded with an acquisition time of 30 s. For the crystal structure determination, the powder, produced by grinding the extracted particles was analyzed by X-ray diffraction (XRD) using a Phillips X' Pert 3040 diffractometer with CuK$\alpha$ radiation; the lattice parameters (see **Table 2**) were obtained by Nelson-Riley analysis.

## 3. Results and Discussion

**Figure 2** shows the cooling curve obtained for the alloy 1 cooled at a rate of ~1˚C/s; its first derivative is also included. Each thermal arrest in the cooling curve is associated with the formation temperature of a microstructural phase; the corresponding $T_p$ was estimated with the aid of an associated peak appearing in the first derivative curve (dotted line in **Figure 2**). According to microstructural observation of the cross area of the alloy 1, the formation temperature of $\alpha_{sc}$-AlFeMnSi phase (hereinafter denoted as $\alpha_{sc}$) is associated with the first thermal arrest occurring in the curve, the second is related with the formation of primary silicon particles and the last represents the heat release during eutectic reaction. **Figure 3** shows SEM images of the $\alpha_{sc}$ phase formed in alloy 1, the irregular morphology observed in the as-cast samples is shown in **Figure 3(a)**, and the polyhedral morphology observed in the isothermally-treated samples is shown in **Figure 3(b)** and **Figure 3(c)**. In **Figure 3(d)** is shown the whole sample obtained by DTA, in this sample can be seen the irregular morphology of the $\alpha_{sc}$ phase, also can be confirmed that this phase not presents direct physical contact with the oxide film of $\alpha$-$Al_2O_3$ formed in the sample's surface by natural oxidation. The presence of $\alpha$-$Al_2O_3$ in the isothermally-treated samples was confirmed by SEM and XRD, as is shown in **Figure 6(c)**, **Figure 8** and **Figure 10(c)**, shown in the following paragraphs. Additionally, some research suggest that oxides such as $\alpha$-$Al_2O_3$ may be present within oxide films depending on the superheating temperature, in this work 900˚C, which favors the transformation of oxide films from $\gamma$-$Al_2O_3$ to $\alpha$-$Al_2O_3$ [22].

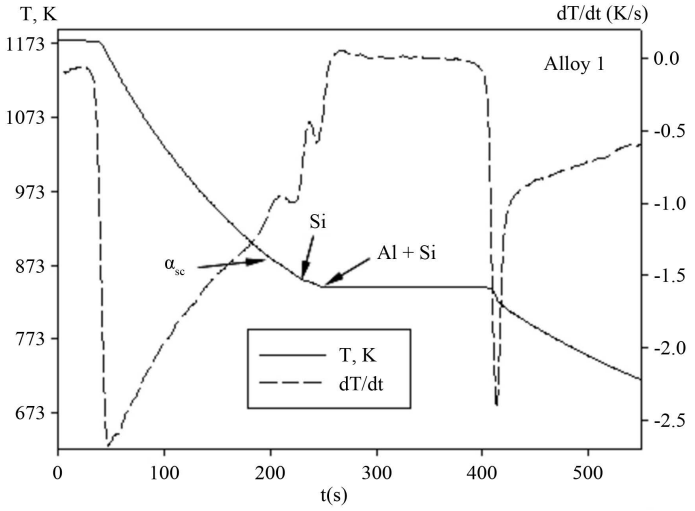


**Figure 2.** Cooling curve and its first derivative for the alloy 1, obtained at an average cooling rate of ~1˚C/s.

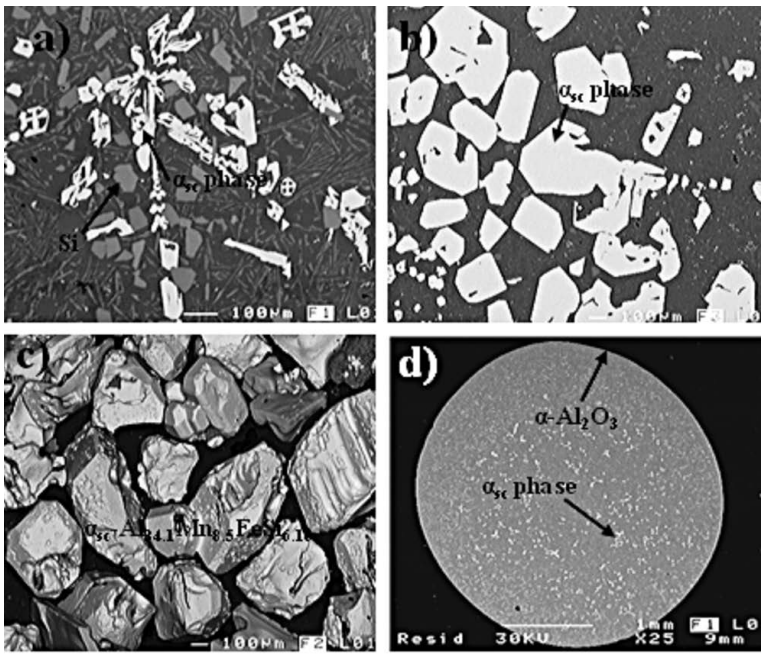


**Figure 3.** SEM micrographs showing the morphology of the $\alpha_{sc}$-AlFeMnSi phase found in alloy 1. (a) As-cast; (b) Isothermally-treated; (c) Extracted $\alpha_{sc}$ particles; (d) DTA sample.

The intermetallics extracted from the isothermally-treated samples of alloy 1 (see **Figure 3(c)**), were analyzed by XRD. As can be observed in **Figure 4**, all peaks correspond to the $Al_{50}Mn_{12}Si_7$ phase (JCPDS card number 71-2182); this phase exhibits a simple cubic (sc) crystal structure with a Pm3 space group [23]. In this work, however, according to the EDS data given in **Table 2**, the extracted intermetallic actually corresponds to the $\alpha_{sc}$-$Al_{34.1}FeMn_{8.5}Si_{6.16}$ formula, with a Fe/Mn weight ratio of 0.12, and a total concentration of transition metals (Fe + Mn) of 32.4%. In comparison, in **Figure 4** are shown the XRD pattern of the $Al_{50}Mn_{12}Si_7$ phase and the experimental XRD pattern of the $\alpha_{sc}$-$Al_{34.1}FeMn_{8.5}Si_{6.16}$ phase. It is observed that both patterns show similar peaks, in some cases the peaks intensity and the $2\theta$ angles change in a little extent. This behavior has been attributable to the substitution of manganese atoms by iron atoms [4] [24] in the lattice sites of the crystal structure. Similar results were observed for the $\alpha_{bcc}$ and $\alpha_h$-AlFeMnSi phases, shown in the following paragraphs.

The cooling curve obtained for the alloy 3 clearly reveals three slope changes during solidification process, as is shown in **Figure 5**. Based on microstructural analysis, the first slope change observed is related with the formation temperature of $\alpha_{bcc}$-AlFeMnSi phase (hereinafter abbreviated as $\alpha_{bcc}$). For the second slope change, the possible reaction indicates the formation of $\beta$-AlFeSi and silicon particles. The $\beta$ phase was not analyzed by XRD due to the small amount formed in the isothermally-treated samples and the fact that it was mixed with the previously formed $\alpha_{bcc}$ phase; however, it was identified as $\beta$ phase based on its typical morphology reported in literature data [25]. Finally, the third slope change is related to the eutectic reaction that is the last to solidify.

SEM micrographs of the $\alpha_{bcc}$ phase are shown in **Figure 6**. The irregular morphology of the $\alpha_{bcc}$ phase can be observed in the as-cast sample (**Figure 6(a)**), and the polyhedral morphology in some intermetallics extracted from the isothermally-treated samples shown in **Figure 6(b)** and **Figure 6(c)**. **Figure 6(c)**, also shows $\alpha_{bcc}$ particles formed on the surface of a $\alpha$-$Al_2O_3$ oxide film, this observation provided the first direct evidence that the $\alpha_{bcc}$ phase can nucleate and grow on the surface of $\alpha$-$Al_2O_3$ oxide films. Figure 6d can be considered as another evidence for the association between $\alpha_{bcc}$ phase and $\alpha$-$Al_2O_3$ oxide films, in this Figure is shown a sample of the alloy 3 obtained by DTA, in the sample can be seen polyhedral $\alpha_{bcc}$ particles revealing that this phase presents direct physical contact with the $\alpha$-$Al_2O_3$ oxide film formed in the sample's surface by natural oxidation.

The XRD pattern of the intermetallic particles extracted from alloy 3 is shown in **Figure 7**. As can be observed, all peaks could be indexed according to the JCPDS card number 71-4015, which corresponds to the $Al_{17}Fe_{3.2}Mn_{0.8}Si_2$ phase. This phase exhibits a body-centered cubic (bcc) crystal structure and belongs to the Im3 space group [26]. For alloy 3, according to the EDS analysis given in **Table 2**, the extracted intermetallic par-

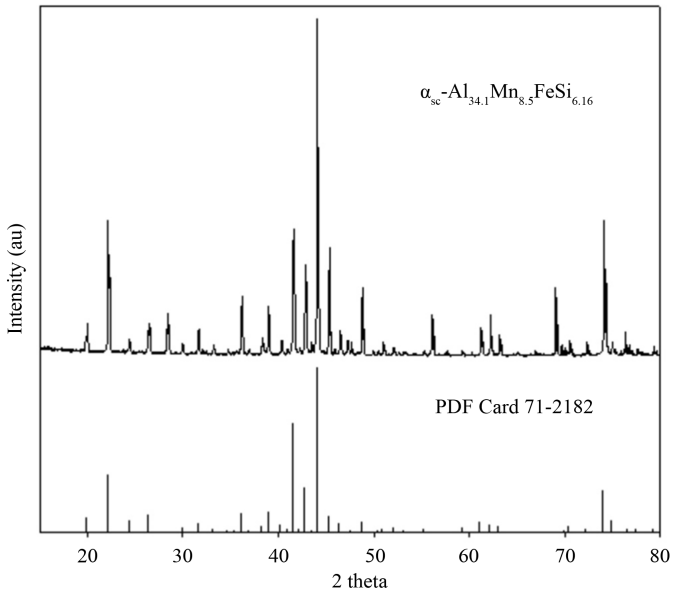


**Figure 4.** XRD pattern obtained for the $\alpha_{sc}$-$Al_{34.1}FeMn_{8.5}Si_{6.16}$ phase extracted from alloy 1.

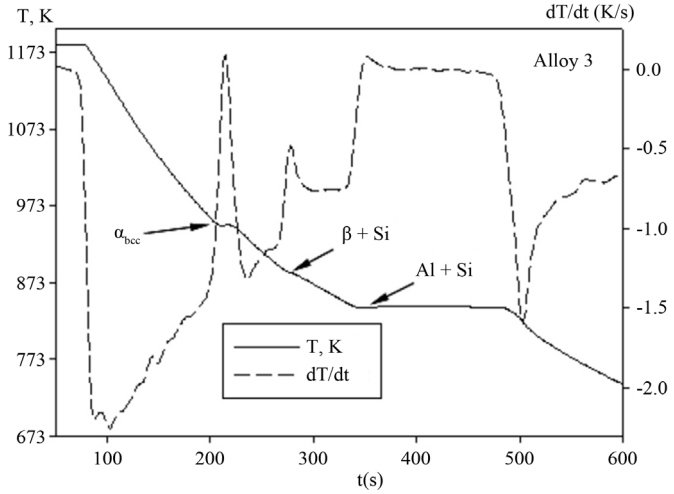


**Figure 5.** Cooling curve and its first derivative for the alloy 3, obtained at an average cooling rate of ~1˚C/s.

ticles corresponded to the $\alpha_{bcc}$-$Al_{8.8}Fe_{1.36}MnSi_{1.47}$ formula. Also, the EDS data given show that the iron contained in the $\alpha_{bcc}$ phase increased, while the manganese contained decreased with increasing iron content in the alloy. The total concentration of transition metals (Fe + Mn) in the $\alpha_{bcc}$ phase fell in the range of 31% - 32%, when iron was added to the alloys. The Fe/Mn weight ratio was in the range of 0.45 - 1.39 for the extracted $\alpha_{bcc}$ phase, therefore the Fe/Mn weight ratio depended on the alloy's chemical composition. It is noteworthy that similar results were obtained for the alloy 2 shown in **Table 2**.

XRD results also shown the presence of $\alpha$-$Al_2O_3$ in the powder produced by grinding the extracted particles from alloys 3 and 4, the last described in the following paragraphs. As observed in **Figure 8**, all peaks of the experimental XRD pattern of the $\alpha$-$Al_2O_3$ were indexed according to the JCPDS card number 74-1081, which corresponds to the $\alpha$-$Al_2O_3$ with a hexagonal crystal structure and R-3c space group [27]. It is worth mentioning that the alumina sample was obtained by separating $\alpha$ phases and alumina particles from particles like those observed in **Figure 6(c)** and **Figure 10(c)**. Such $\alpha$-$Al_2O_3$ particles have been thought to originate during casting of the melt into the graphite crucible and subsequent melt superheating at 900˚C.

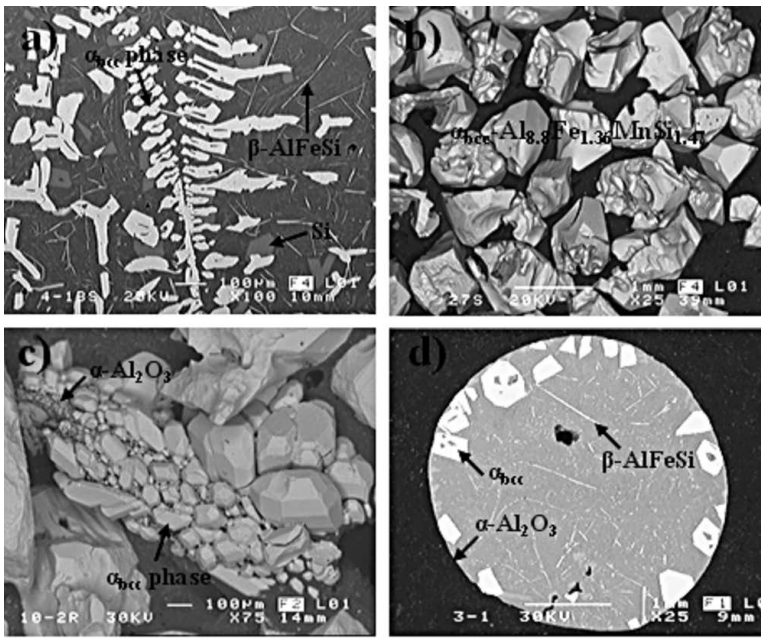


**Figure 6.** SEM micrographs showing the morphology of the $\alpha_{bcc}$-AlFeMnSi phase found in alloy 3. (a) As-cast; (b) Extracted $\alpha_{bcc}$ particles; (c) $\alpha_{bcc}$ particles formed on $\alpha$-$Al_2O_3$ oxide film; (d) DTA sample.

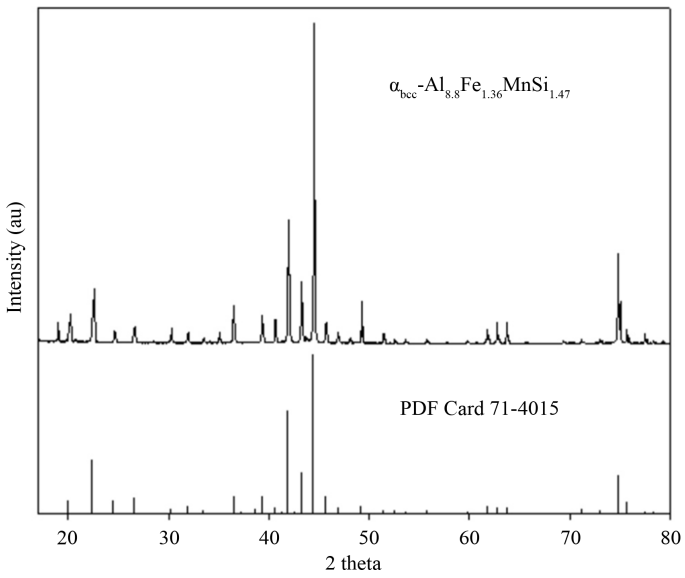


**Figure 7.** XRD pattern obtained for the $\alpha_{bcc}$-$Al_{8.8}Fe_{1.36}MnSi_{1.47}$ phase extracted from alloy 3.

The results of the alloy 4 (**Figure 9**) indicate that there are two Fe-rich intermetallic phases prior to the eutectic reaction. The primary phase for this alloy was $\alpha_h$-AlFeMnSi (hereinafter denoted as $\alpha_h$), which is associated to the first slope change. The second slope change represents the formation temperature of $\beta$-AlFeSi phase and some silicon particles. Finally, the last slope change represents the heat release during the eutectic reaction. SEM images of the $\alpha_h$ phase revealed that this phase exhibits irregular morphology in the as-cast samples (**Figure 10(a)**), and polyhedral morphology in the isothermally-treated samples, as can be seen in the intermetallics extracted shown in **Figure 10(c)**. In this Figure, also can be observed that $\alpha_h$ particles are formed on the surface of a $\alpha$-$Al_2O_3$ oxide film. This microstructural observation provided direct evidence that confirms that the $\alpha_h$ phase

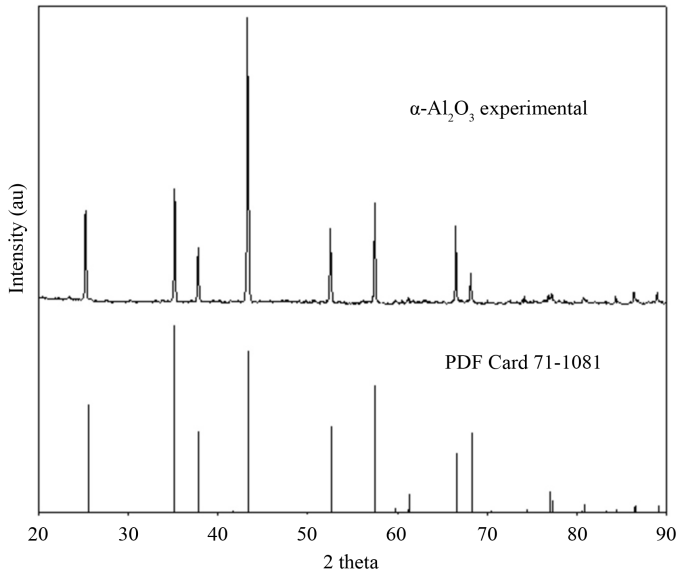


**Figure 8.** XRD pattern obtained for the $\alpha$-$Al_2O_3$ formed by natural oxidation in the experimental aluminum alloys.

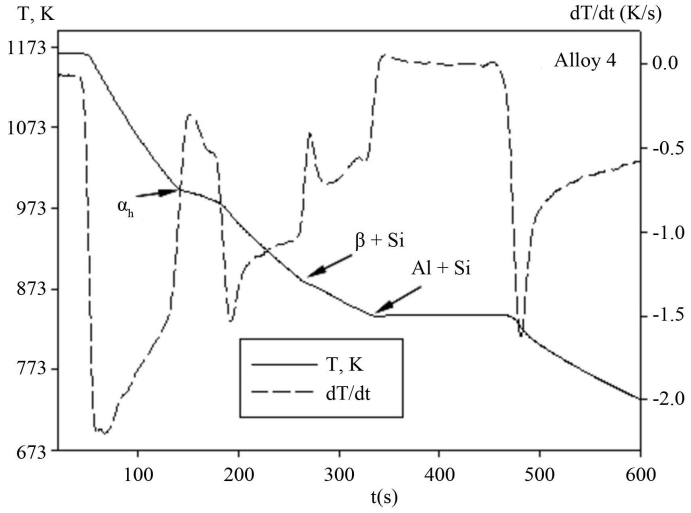


**Figure 9.** Cooling curve and its first derivative for the alloy 4, obtained at an average cooling rate of ~1˚C/s.

can nucleate and grow on the wetted surface of $\alpha$-$Al_2O_3$ oxide films. **Figure 10(d)** shown a sample of the alloy 4 obtained by DTA, this sample has revealed that $\alpha_h$ particles with polyhedral morphology are located on the wetted surface of the oxide film formed in the sample's surface by natural oxidation, so can be established that the $\alpha_h$ phase presents direct physical contact with the $\alpha$-$Al_2O_3$ oxide film. This observation can support the association between $\alpha_h$ phase and $\alpha$-$Al_2O_3$ oxide film.

The intermetallic particles extracted from isothermally-treated samples of alloy 4, were analyzed by XRD. As observed in **Figure 11**, all peaks of the experimental XRD pattern were indexed according to the JCPDS card number 71-0238, which corresponds to the $Al_{167.8}Fe_{44.9}Si_{23.9}$ phase. This phase exhibits a hexagonal crystal structure, and belongs to the P63/mmc space group [28]. In this work, however, the chemical composition of the extracted intermetallic corresponded to the $\alpha_h$-$Al_{14}Fe_{3.36}MnSi_{3.15}$ formula according to **Table 2**. EDS data of the $\alpha_h$ phase revealed that the total concentration of transition metals (Fe + Mn) in the $\alpha_h$ phase fell in the range of 33.3% - 34.2%. The Fe/Mn weight ratio was in the range of 3.41 - 4.22 for the extracted $\alpha_h$ phase so can be es-

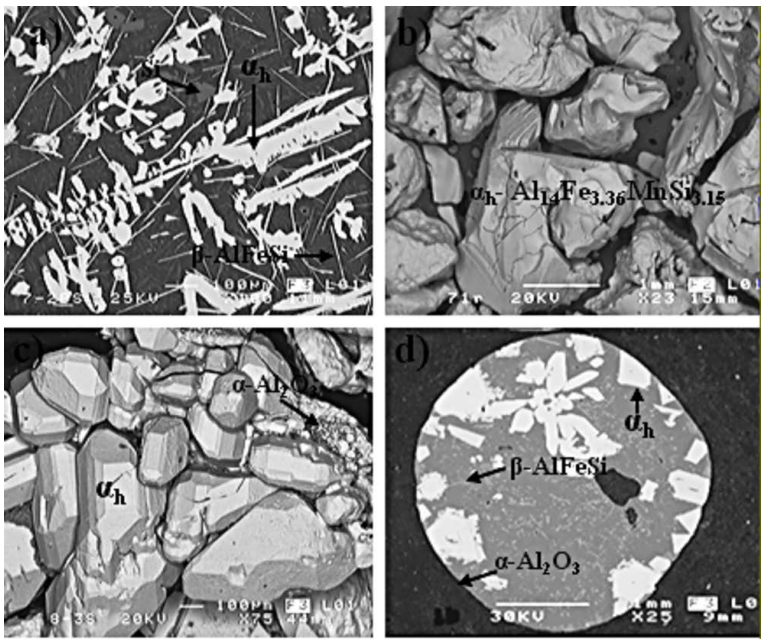


**Figure 10.** SEM micrographs showing the morphology of the $\alpha_h$-AlFeMnSi phase found in alloy 4. (a) As-cast; (b) Extracted $\alpha_h$ phase; (c) $\alpha_h$ particles formed on $\alpha$-$Al_2O_3$ oxide film; (d) DTA sample.

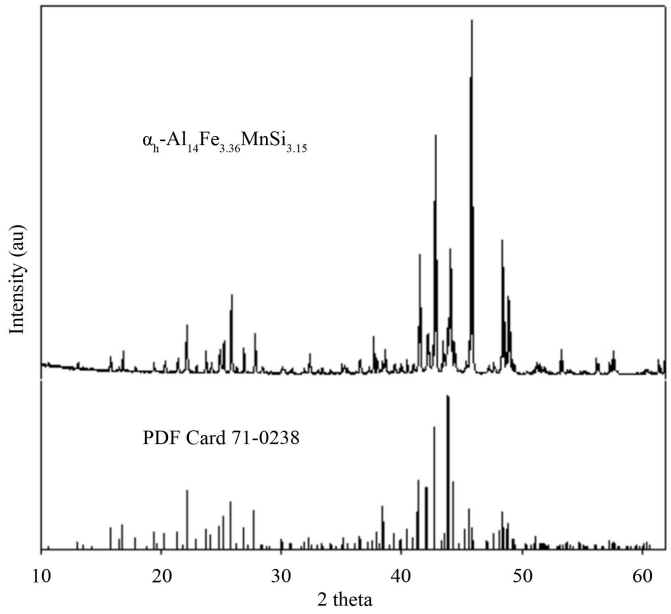


**Figure 11.** XRD pattern obtained for the $\alpha_h$-$Al_{14}Fe_{3.36}MnSi_{3.15}$ phase extracted from alloy 4.

tablished that the Fe/Mn weight ratio depended on the alloy's chemical composition. It is worth mentioning that similar results were observed for the alloy 5 shown in **Table 2**.

Based on microstructural observation there is good experimental evidence that led us to assume that the $\alpha_{bcc}$ and $\alpha_h$ phases present direct physical contact with the $\alpha$-$Al_2O_3$ oxide films, as is shown in **Figure 6(c)** and **Figure 10(c)**. If $\alpha_{bcc}$ and $\alpha_h$ phases nucleate and grow on the wetted surface of $\alpha$-$Al_2O_3$ oxide films, it is expected that there will be good atomic contact and good lattice match between the wetted surface of $\alpha$-$Al_2O_3$ oxide films and the $\alpha_{bcc}$ and $\alpha_h$ particles that have grown on it. This assumption led us to suggesting that $\alpha$-$Al_2O_3$ oxide films

act as a preferential nucleation site for $\alpha_{bcc}$ and $\alpha_h$ phases due to the similarity in their crystal structure. Also, if $\alpha$-$Al_2O_3$ oxide film is a good nucleant for $\alpha_{bcc}$ and $\alpha_h$ phases, it is expected that it will determine the spatial distribution of these phases, as can be observed in **Figure 6(d)** and **Figure 10(d)**, where the $\alpha_{bcc}$ and $\alpha_h$ particles are located on the oxidized melt surface in DTA samples of alloys 3 and 4. This observation tends to support the assumption that $\alpha$-$Al_2O_3$ oxide films act as a preferential nucleation site for $\alpha_{bcc}$ and $\alpha_h$ phases.

Careful studies of crystallographic orientation relationships may be another way to confirm that $\alpha$-$Al_2O_3$ oxide film is a good nucleant for $\alpha_{bcc}$ and $\alpha_h$ phases. In general, it is accepted that the mismatch of crystal structures, the electronic nature of the crystal bonds of the two phases, superheating, and the presence of alloying elements are factors that may influence the favorability of nucleation.

On the other hand, for the $\beta$ phase formed in the experimental alloys, was not found direct physical contact with the $\alpha$-$Al_2O_3$ oxide film formed in the sample's surface by natural oxidation, as can be seen in **Figure 6(d)** and **Figure 9(d)**. This observation led us to assume that between the $\beta$ phase and $\alpha$-$Al_2O_3$ oxide films there is not good atomic contact and good lattice match, thus, the $\beta$ phase did not appear to nucleate and grow on the surface of $\alpha$-$Al_2O_3$ oxide films.

According to the Mn content of the studied alloys could be expected the formation of $MnO{\cdot}Al_2O_3$, $Mn_2O_3$, or $MnO{\cdot}SiO_2$ particles, however, the presence of these oxides was not detected by X-ray diffraction, as can be seen in **Figure 8**. Another effect that could be expected is that Mn content had an effect on the alumina transformation from $\gamma$-$Al_2O_3$ to $\alpha$-$Al_2O_3$, nonetheless, according to the experimental XRD pattern of the $\alpha$-$Al_2O_3$, shown in **Figure 8**, such effect was discarded for the studied temperature range. Thus, it was thought that Mn content just become embedded in the solidification of the $\alpha_{sc}$, $\alpha_{bcc}$ and $\alpha_h$ phases. This observation is in accordance with some research [4] [24], that suggest that many ternary AlFeSi intermetallics can accept Mn atoms into solid solution, which reflects the fact that Mn atoms may replace the Fe atoms in their crystal structure. Finally, it is important study whether the Fe-rich intermetallic phases can nucleate at all without the presence of oxide films in aluminum melts. This important question is not easily answered because obtaining aluminum melts free from oxide films remains difficult.

## 4. Conclusion

According to the experimental results, it can be established that the $\alpha_{bcc}$ and $\alpha_h$ phases nucleate and grow on the wetted surface of $\alpha$-$Al_2O_3$ oxide films formed by natural oxidation in aluminum melts. On the other hand, the $\beta$ particles formed in the experimental alloys not presents direct physical contact with the $\alpha$-$Al_2O_3$ oxide films, thus, the $\beta$ phase did not appear to nucleate on $\alpha$-$Al_2O_3$ oxide films.

## Acknowledgements

The authors are grateful to the National Council for Science and Technology of Mexico (Conacyt) for the financial support provided to carry out this work (Project No. 149030).

## References

[1] Preston, R.S. and Gerlach, R. (1971) Mössbauer Effect in Dilute Alloys of Iron in Aluminum. *Physical Review B*, **3**, 1519. http://dx.doi.org/10.1103/PhysRevB.3.1519

[2] Stefaniay, V., Griger, A. and Turmezey, T. (1987) Intermetallic Phases in the Aluminium-Side Corner of the AlFeSi-Alloy System. *Journal of Materials Science*, **22**, 539-546. http://dx.doi.org/10.1007/BF01160766

[3] Crepeau, P.N. (1995) Effect of Iron in Al-Si Casting Alloys: A Critical Review. *AFS Transactions*, **103**, 361-366.

[4] Kuijpers, N.C.W., Vermolen, F.J., Vuik, C., Koenis, P.T.G., Nilsen, K.E. and van Zwaag, S. (2005) The Dependence of the $\beta$-AlFeSi to $\alpha$-Al(FeMn)Si Transformation Kinetics in Al-Mg-Si Alloys on the Alloying Elements. *Materials Science and Engineering A*, **394**, 9-19. http://dx.doi.org/10.1016/j.msea.2004.09.073

[5] Backerud, L., Król, E. and Tamminen, J. (1986) Solidification Characteristics of Aluminum Alloys. Vol. 1, AFS/Skanaluminum, Oslo.

[6] Kral, M.V., Nakashima, P.N.H. and Mitchell, D.R.G. (2006) Electron Microscope Studies of Al-Fe-Si Intermetallics in an Al-11 Pct Si Alloy. *Metallurgical and Materials Transactions A*, **37A**, 1987-1997. http://dx.doi.org/10.1007/s11661-006-0141-8

[7] Tibballs, J.E., Horst, J.A. and Simensen, C.J. (2001) Precipitation of $\alpha$-Al(Fe,Mn)Si from the Melt. *Journal of Mate-*

*rials Science*, **36**, 937-941. http://dx.doi.org/10.1023/A:1004815621313

[8] Mondolfo, L.F. (1976) Aluminum Alloys: Structure and Properties. Butterworths and Co., Ltd., London, 806. http://dx.doi.org/10.1016/B978-0-408-70932-3.50404-6

[9] Barlock, J.G. and Mondolfo, L.F. (1975) Structure of Some Aluminium-Iron-Magnesium-Manganesesilicon Alloys. *Zeitschrift Fur Metallkunde*, **66**, 605.

[10] Corby, R.N. and Black, P.J. (1977) The Structure of Aluminum-Iron-Silicon ($\alpha$-(A1FeSi)) by Anomalous-Dispersion Methods. *Acta Crystallographica Section B*, **33**, 3468-3475. http://dx.doi.org/10.1107/S0567740877011224

[11] Murali, S., Raman, K.S. and Murthy, K.S.S. (1992) Effect of Magnesium, Iron (Impurity) and Solidification Rates on the Fracture Toughness of Al-7Si-0.3Mg Casting Alloy. *Materials Science and Engineering*: *A*, **151**, 1-10. http://dx.doi.org/10.1016/0921-5093(92)90175-Z

[12] Shabestari, S. and Gruzleski, J.E. (1995) Gravity Segregation of Complex Intermetallics Compounds in Liquid Aluminum-Silicon Alloy. *Metallurgical and Materials Transactions A*, **26**, 999-1006. http://dx.doi.org/10.1007/BF02649097

[13] Romming, C., Hansen, V. and Gjonnes, J. (1994) Crystal Structure of $\beta$-$Al_{4.5}FeSi$. *Acta Crystallographica Section B*, **50**, 307-312. http://dx.doi.org/10.1107/S0108768193013096

[14] Mulazimoglu, M.H., Zaluska, A., Gruzleski, J.E. and Paray, F. (1996) Electron Microscope Study of Al-Fe-Si Intermetallics in 6201 Aluminum Alloy. *Metallurgical and Materials Transactions A*, **27**, 929-936. http://dx.doi.org/10.1007/BF02649760

[15] Vybornov, M., Rogl, P. and Sommer, F. (1997) On the Thermodynamic Stability and Solid Solution Behavior of the Phases $\tau_5$-$Fe_2Al_{7.4}Si$ and $\tau_6$-$Fe_2Al_9Si_2$. *Journal of Alloys and Compounds*, **247**, 154-157. http://dx.doi.org/10.1016/S0925-8388(96)02602-3

[16] Shabestari, S.G., Mahmudi, M., Emamy, M. and Campbell, J. (2002) Effect of Mn and Sr on Intermetallics in Fe-Rich Eutectic Al-Si Alloy. *International Journal of Cast Metals Research*, **15**, 17-24.

[17] Cao, X. and Campbell, J. (2004) Effect of Sr on Primary $\alpha$-Fe Phase in Liquid Al-$_{11.5}$Si-$_{0.4}$Mg Cast Alloy. *Materials Science and Technology*, **20**, 514-520.

[18] Cao, X. and Campbell, J. (2004) The Solidification Characteristics of Fe-Rich Intermetallics in Al-$_{11.5}$Si-$_{0.4}$-Mg Cast Alloy. *Metallurgical and Materials Transactions A*, **35**, 1425-1435. http://dx.doi.org/10.1007/s11661-004-0251-0

[19] Miller, D.N., Lu, L. and Dahle, A.K. (2006) The Role of Oxides in the Formation of Primary Ironintermetallics in an Al-$_{11.6}$Si-$_{0.37}$Mg Alloy. *Metallurgical and Materials Transactions B*, **37**, 873-878. http://dx.doi.org/10.1007/BF02735008

[20] Khalifa, W., Samuel, F.H., Gruzleski, J.E., Doty, H.W. and Valtierra, S. (2005) Nucleation of Fe-Intemetallics Phases in the Al-Fe-Si Alloys. *Metallurgical and Materials Transactions A*, **36**, 1017-1032. http://dx.doi.org/10.1007/s11661-005-0295-9

[21] Lu, L. and Dahle, A.K. (2005) Iron-Rich Intermetallics Phases and Their Role in Castings Defect Formation in Hypoeutectic Al-Si Alloys. *Metallurgical and Materials Transactions A*, **36**, 819-835.

[22] Anantha Narayanan, L., Samuel, F.H. and Gruzleski, J.E. (1994) Crystallization Behavior of Iron Containing Intermetallics Compounds in 319 Aluminum Alloy. *Metallurgical and Materials Transactions A*, **25**, 1761-1773. http://dx.doi.org/10.1007/BF02668540

[23] Cooper, M. and Robinson, K. (1966) The Crystal Structure of the Ternary Alloy $\alpha$ (AlMnSi). *Acta Crystallographica*, **20**, 614-617. http://dx.doi.org/10.1107/S0365110X6600149X

[24] Schurer, P.J., Koopmans, B. and Van der Woude, F. (1988) Structure of Icosahedral Al-($M_{1-x}Fe_x$) Alloys ($M$ = Cr, Mn, or Fe). *Physical Review B*, **37**, 507-510. http://dx.doi.org/10.1103/PhysRevB.37.507

[25] Rivlin, V.G. and Raynor, G.V. (1981) Critical Evaluation of Constitution of Al-Fe-Si System. *International Metals Reviews*, **26**, 133-152.

[26] Cooper, M. (1967) The Crystal Structure of the Ternary Alloy $\alpha$ (AlFeSi). *Acta Crystallographica*, **23**, 1106-1107. http://dx.doi.org/10.1107/S0365110X67004372

[27] Saalfeld, H. (1964) The Crystal Chemistry of $Al_2O_3$-$Cr_2O_3$. *Zeitschrift für Kristallographie—Crystalline Materials*, **120**, 342-348. http://dx.doi.org/10.1524/zkri.1964.120.4-5.342

[28] Corby, R.N. and Black, P.J. (1977) The Structure of $\alpha$-(AlFeSi) by Anomalous-Dispersion Methods. *Acta Crystallographica Section B*, **33**, 3468-3475. http://dx.doi.org/10.1107/S0567740877011224

Scientific Research Publishing (SCIRP) is one of the largest Open Access journal publishers. It is currently publishing more than 200 open access, online, peer-reviewed journals covering a wide range of academic disciplines. SCIRP serves the worldwide academic communities and contributes to the progress and application of science with its publication.

**Other selected journals from SCIRP are listed as below. Submit your manuscript to us via either submit@scirp.org or Online Submission Portal.**